DISSERTATION

EMERGENT TOPOLOGICAL PHENOMENA IN LOW-D SYSTEMS INDUCED BY GAUGE

POTENTIALS

Submitted by

Aidan Winblad

Department of Physics

In partial fulfillment of the requirements

For the Degree of Doctor of Philosophy

Colorado State University

Fort Collins, Colorado

Fall 2023

Doctoral Committee:

    Advisor: Hua Chen

    Richard Eykholt
    Martin Gelfand
    Olivier Pinaud

ABSTRACT

EMERGENT TOPOLOGICAL PHENOMENA IN LOW-D SYSTEMS INDUCED BY GAUGE

POTENTIALS

Abstract goes here

ACKNOWLEDGEMENTS

DEDICATION

I would like to dedicate this dissertation to my dog Zeta.

TABLE OF CONTENTS

LIST OF TABLES

LIST OF FIGURES

Chapter 1

Introduction

EM gauge potential appears in electronic Hamiltonian in CM

1. Review Maxwell theory -> gauge potential

2. Minimal coupling $-i\hbar\nabla \to -i\hbar\nabla + q\mathbf{A}$ or $-i\partial_\mu \to -i\partial_\mu + qA_\mu$

3. TB Hamiltonian and Peierls phase

Topological phenomena in CM considered in thesis

1. (1) Majorana and TSC

    i Kitaev chain (M— topological invariant). BdG?

    ii Braiding (Application in TQC)

2. Landau Level and Hofstadter butterfly

    i solve for LL in 2DEG — why it's topological, chern number, TKNN quantum Hall

    ii square lattice — hofstadter butterfly (on other lattices, honeycomb)

Chapter 2

Superconducting Triangular Islands as a Platform for Manipulating Majorana Zero Modes

2.1 Introduction

For more than twenty years, Majorana zero modes (MZM) in condensed matter systems have been highly sought after due to their potential for serving as building blocks of topological quantum computation, thanks to their inherent robustness against decoherence and non-Abelian exchange statistics [?, ?, ?, ?, ?]. MZM were originally proposed to be found in half-quantum vortices of two-dimensional (2D) topological p-wave superconductors and at the ends of 1D spinless p-wave superconductors [?, ?]. Whether a pristine p-wave superconductor [?] has been found is still under debate. However, innovative heterostructures proximate to ordinary s-wave superconductors have been proposed to behave as effective topological superconductors in both 1D and 2D. These include, for example, semiconductor nanowires subject to magnetic fields [?, ?, ?], ferromagnetic atomic spin chains [?, ?, ?, ?, ?, ?], 3D topological insulators [?, ?, ?, ?], quantum anomalous Hall insulators [?, ?, ?], quasi-2D spin-orbit-coupled superconductors with a perpendicular Zeeman field [?, ?, ?, ?, ?, ?], and planar Josephson junctions [?, ?, ?, ?, ?, ?, ?], etc. It has been a challenging task to decisively confirm the existence of MZM in the various experimental systems due to other competing mechanisms that can potentially result in similar features as MZM do in different probes [?, ?, ?, ?, ?, ?, ?, ?]. Other proposals for constructing Kitaev chains through a bottom-up approach, based on, e.g. magnetic tunnel junctions proximate to spin-orbit-coupled superconductors [?], and quantum dots coupled through superconducting links [?, ?, ?] are therefore promising. In particular, the recent experiment [?] of a designer minimal Kitaev chain based on two quantum dots coupled through tunable crossed Andreev reflections (CAR) offers a compelling route towards MZM platforms based on exactly solvable building blocks.

In parallel with the above efforts of realizing MZM in different materials systems, scalable architectures for quantum logic circuits based on MZM have also been intensely studied over the past decades. A major proposal among these studies is to build networks of T-junctions, which are minimal units for swapping a pair of MZM hosted at different ends of a junction, that allow braiding-based TQC [**?**]. Alternatively, networks based on coupled wires forming the so-called tetrons and hexons, aiming at measurement-based logic gate operations [**?**], have also been extensively investigated. To counter the technical challenges of engineering networks with physical wires or atomic chains, various ideas based on effective Kitaev chains, such as quasi-1D systems in thin films [**?**], cross Josephson junctions [**?**], scissor cuts on a quantum anomalous Hall insulator [**?**], and rings of magnetic atoms [**?**], etc. have been proposed. However, due to the same difficulty of obtaining or identifying genuine MZM in quasi-1D systems mentioned above, it remains unclear how practical these strategies are in the near future.

In this Letter, we propose an alternative structural unit for manipulating MZM, triangular superconducting islands, motivated by the above challenges associated with wire geometries and by the fact that triangular islands routinely appear spontaneously in epitaxial growth [**?**] on close-packed atomic surfaces. We first show that a minimal "Kitaev triangle" consisting of three sites hosts MZM at different pairs of vertices controlled by Peierls phases on the three edges [Fig. 2.1 (a)], which can be readily realized using quantum dots. To generalize the minimal model to triangular structures involving more degrees of freedom, we study the topological phase transitions of quasi-1D ribbons driven by Peierls phases, which can be created by magnetic fields or supercurrents [**?, ?**], and use the resulting phase diagram as a guide to construct finite-size triangles with a hollow interior that host MZM [Fig. 2.1 (b)]. In the end we discuss possible experimental systems that can realize our proposals and scaled-up networks of triangles for implementing braiding operations of MZM.
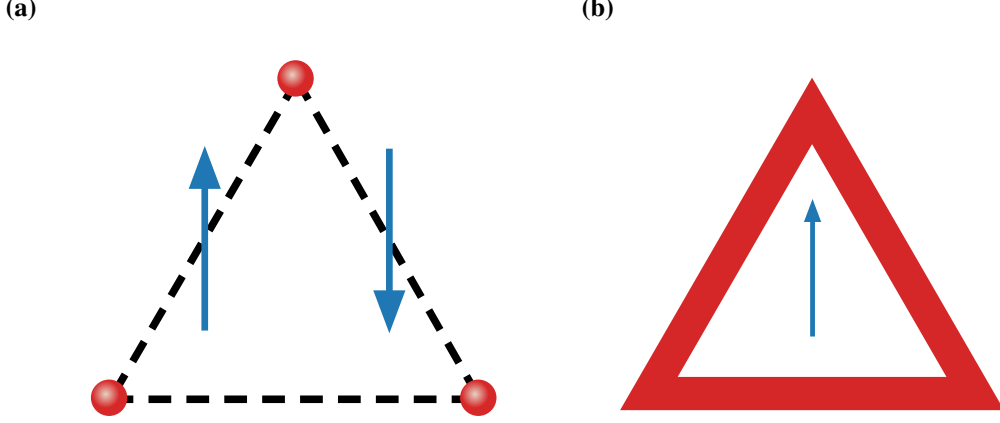
Figure 2.1: Schematics of two triangle structures proposed in this work. (a) Three-site Kitaev triangle with bond-dependent Peierls phases. (b) Hollow triangular island with a uniform vector potential.

2.2   Kitaev Triangle

In this section we present an exactly solvable minimal model with three sites forming a "Kitaev triangle" that can host MZM at different pairs of vertices controlled by Peierls phases on the edges. The Bogoliubov-de Gennes (BdG) Hamiltonian includes complex hopping and p-wave pairing between three spinless fermions forming an equilateral triangle [Fig. 2.1 (a)]:

$$\mathcal{H} = \sum_{\langle jl \rangle}(-te^{i\phi_{jl}}c_j^\dagger c_l + \Delta e^{i\theta_{jl}}c_j c_l + \text{h.c.}) - \sum_j \mu c_j^\dagger c_j, \tag{2.1}$$

where t is the hopping amplitude, Δ is the amplitude of the (2D) p-wave pairing, μ is the chemical potential, θ_{jl} is the polar angle of $\mathbf{r}_{jl} = \mathbf{r}_l - \mathbf{r}_j$ (the x axis is chosen to be along $\mathbf{r}_{12}$), consistent with $\{c_l^\dagger, c_j^\dagger\} = 0$. ϕ_{jl} is the Peierls phase due to a bond-dependent vector potential $\mathbf{A}$ to be specified below (the nearest neighbor distance a is chosen to be the length unit hereinbelow):

$$\phi_{jl} = \frac{e}{\hbar}\int_{\mathbf{r}_j}^{\mathbf{r}_l} \mathbf{A} \cdot d\mathbf{l} = -\phi_{lj} \tag{2.2}$$

where $e > 0$ is the absolute value of the electron charge. Below we use the natural units $e = \hbar = 1$. To get the conditions for having MZM in this model we rewrite $\mathcal{H}$ in the Majorana fermion basis

$a_j = c_j + c_j^\dagger$, $b_j = \frac{1}{i}(c_j - c_j^\dagger)$:

$$\mathcal{H} = -\frac{i}{2} \sum_{\langle jl \rangle} \Big[(t \sin\phi_{jl} - \Delta \sin\theta_{jl}) \, a_j a_l \tag{2.3}$$

$$+ (t \sin\phi_{jl} + \Delta \sin\theta_{jl}) \, b_j b_l$$

$$+ (t \cos\phi_{jl} - \Delta \cos\theta_{jl}) \, a_j b_l$$

$$- (t \cos\phi_{jl} + \Delta \cos\theta_{jl}) \, b_j a_l \Big] - \frac{i\mu}{2} \sum_j a_j b_j$$

For concreteness we consider the Kitaev limit $t = \Delta$, $\mu = 0$, and choose $\phi_{12} = 0$ so that sites 1 and 2 alone form a minimal Kitaev chain with $\mathcal{H}_{12} = it b_1 a_2$ and hosting MZM a_1 and b_2. In order for the MZM to persist in the presence of site 3, one can choose ϕ_{23} and ϕ_{31} so that all terms involving these Majorana operators cancel out. For example, consider the $2-3$ bond, for which $\theta_{23} = 2\pi/3$, we require

$$\sin\phi_{23} + \sin\frac{2\pi}{3} = \cos\phi_{23} + \cos\frac{2\pi}{3} = 0 \tag{2.4}$$

which means $\phi_{23} = -\pi/3$. Similarly one can find $\phi_{31} = -\phi_{13} = -\pi/3$. The three Peierls phases can be realized by the following staggered vector potential

$$\mathbf{A} = [1 - 2\Theta(x)] \frac{2\pi}{3\sqrt{3}} \hat{\mathbf{y}} \tag{2.5}$$

where $\Theta(x)$ is the Heavisde step function. In fact, using a uniform $\mathbf{A} = \frac{2\pi}{3\sqrt{3}}\hat{\mathbf{y}}$, which corresponds to $\phi_{23} = -\pi/3 = -\phi_{31}$ also works, since the existence of a_1 is unaffected by ϕ_{23}. However, in this case the counterpart of b_2 is not localized on a single site. For the same reason, the above condition for MZM localized at triangle corners can be generalized to Kitaev chains forming a triangular loop, as well as to finite-size triangles of 2D spinless p-wave superconductors in the Kitaev limit, as the existence of a_1 and b_2 are only dictated by the vector potential near the corresponding corners.

It should be noted that in the latter case, 1D Majorana edge states will arise when the triangle becomes larger, and effectively diminish the gap that protects the corner MZM. On the other hand, for the longer Kitaev chain, due to the potential practical difficulty of controlling further-neighbor hopping and pairing amplitudes, it is better to resort to the approach of controlling the individual topological phases of the three edges which will be detailed in the next section.

We next show that the minimal Kitaev triangle suffices to demonstrate braiding of MZM. To this end we consider a closed parameter path linearly interpolating between the following sets of values of ϕ_{jl}:

$$
\begin{aligned}
(\phi_{12}, \phi_{23}, \phi_{31}) \quad &= \quad \left(0, -\frac{\pi}{3}, -\frac{\pi}{3}\right) \equiv \boldsymbol{\phi}_1 \\
&\rightarrow \quad \left(-\frac{\pi}{3}, -\frac{\pi}{3}, 0\right) \equiv \boldsymbol{\phi}_2 \\
&\rightarrow \quad \left(-\frac{\pi}{3}, 0, -\frac{\pi}{3}\right) \equiv \boldsymbol{\phi}_3 \\
&\rightarrow \quad \boldsymbol{\phi}_1
\end{aligned}
\tag{2.6}
$$

It is straightforward to show that at $\boldsymbol{\phi}_2$ and $\boldsymbol{\phi}_3$ there are MZM located at sites $3, 1$ and $2, 3$, respectively. Therefore the two original MZM at sites $1, 2$ should switch their positions at the end of the adiabatic evolution.

Indeed, Fig. 2.2 shows that the MZM stays at zero energy throughout the parameter path that interchanges their positions. To show that such an operation indeed realizes braiding, we explicitly calculated the many-body Berry phase of the evolution [**?**,**?**,**?**] and found the two degenerate many-body ground states acquire a $\frac{\pi}{2}$ difference in their Berry phases as expected [**?**]. Compared to the minimum T-junction model with four sites [**?**], our Kitaev triangle model only requires three sites to achieve braiding between two MZM, and is potentially also easier to engineer experimentally. In the next section we will show that a more mesoscopic hollow-triangle structure can achieve similar results and may be preferred in other materials platforms.
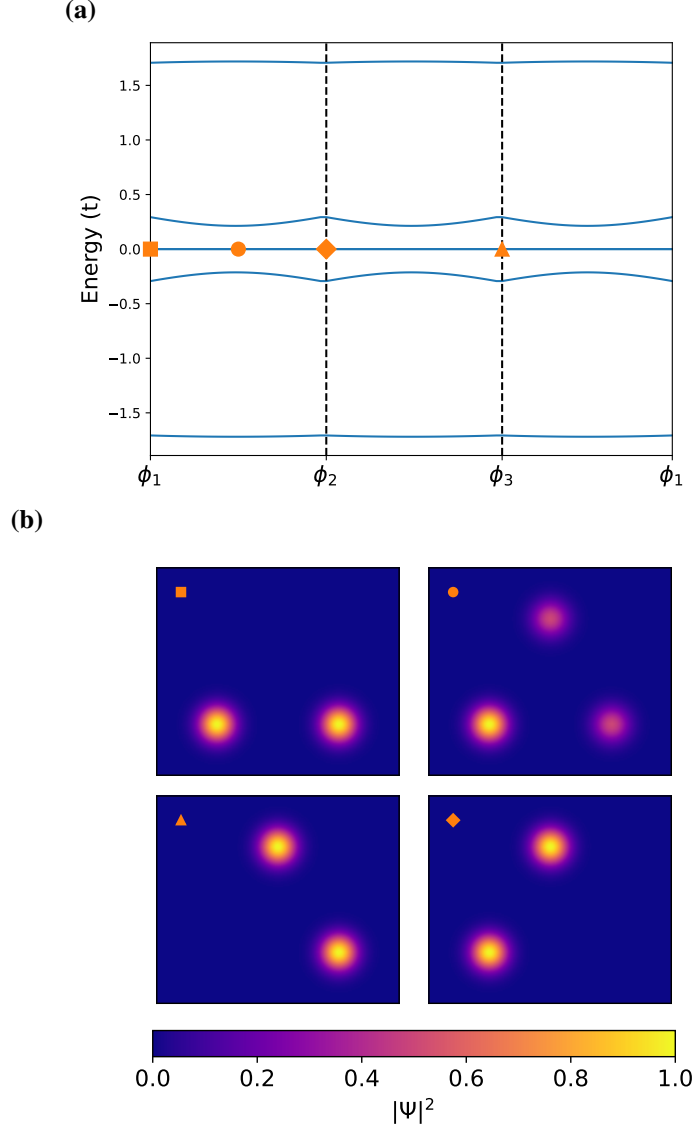
Figure 2.2: (a) Evolution of the eigenvalues of the 3-site Kitaev triangle along the closed parameter path for ϕ on the three edges. (b) MZM wavefunctions at different points of the parameter path. Clockwise from the upper left panel: $\phi_1 \to \frac{1}{2}(\phi_1 + \phi_2) \to \phi_2 \to \phi_3$.

2.3 Hollow Triangles

For systems with less fine-tuned Hamiltonians than the minimal model in the previous section, it is more instructive to search for MZM based on topological arguments. In this section we show that MZM generally appear at the corners of a hollow triangle, which can be approximated by joining three finite-width chains or ribbons whose bulk topology is individually tuned by the same uniform vector potential.

7

To this end, we first show that topological phase transitions can be induced by a vector potential in a spinless p-wave superconductor ribbon. In comparison with similar previous proposals that mostly focused on vector potentials or supercurrents flowing along the chain [?, ?], we consider in particular the tunability by varying the direction of the vector potential relative to the length direction of the ribbon, which will become instrumental in a triangular structure.

Consider Eq. (A.2) on a triangular lattice defined by unit-length lattice vectors $(\mathbf{a}_1, \mathbf{a}_2) = (\hat{\mathbf{x}}, \frac{1}{2}\hat{\mathbf{x}} + \frac{\sqrt{3}}{2}\hat{\mathbf{y}})$ with W unit cells along $\mathbf{a}_2$ but infinite unit cells along $\mathbf{a}_1$, and assume the Peierls phases are due to a uniform vector potential $\mathbf{A}$ so that $\phi_{jl} = \mathbf{A} \cdot \mathbf{r}_{jl}$. We also introduce $\mathbf{a}_3 \equiv -\mathbf{a}_1 + \mathbf{a}_2$ for later convenience. The Hamiltonian is periodic along x and can be Fourier transformed through $c_{m,n}^\dagger = \frac{1}{\sqrt{N}} \sum_k c_{k,n}^\dagger e^{-ikm}$, where m, n label the lattice sites as $\mathbf{r}_{m,n} = m\mathbf{a}_1 + n\mathbf{a}_2$. The resulting momentum space Hamiltonian can be written as the following block form up to a constant

$$\mathcal{H} = \frac{1}{2} \sum_k \Psi_k^\dagger \begin{pmatrix} h_t(k) & h_\Delta(k) \\ h_\Delta^\dagger(k) & -h_t^*(-k) \end{pmatrix} \Psi_k \tag{2.7}$$

$$\equiv \frac{1}{2} \sum_k \Psi_k^\dagger H(k) \Psi_k$$

where $\Psi_k \equiv (c_{k,1}, \ldots, c_{k,W}, c_{-k,1}^\dagger, \ldots c_{-k,W}^\dagger)^T$. $h_t(k)$ is a $W \times W$ Hermitian tridiagonal matrix with $(h_t)_{n,n} = -2t\cos(k + \mathbf{A} \cdot \mathbf{a}_1) - \mu$ and $(h_t)_{n,n+1} = -t\left(e^{i(-k+\mathbf{A}\cdot\mathbf{a}_3)} + e^{i\mathbf{A}\cdot\mathbf{a}_2}\right)$. $h_\Delta(k)$ is a $W \times W$ tridiagonal matrix with $(h_\Delta)_{n,n} = -2i\Delta\sin k$ and $(h_\Delta)_{n,n\pm1} = \mp\Delta\left[e^{-i(\pm k + \frac{2\pi}{3})} + e^{-i\frac{\pi}{3}}\right]$.

By transforming Eq. (2.7) to the Majorana basis using the unitary transformation:

$$U \equiv \frac{1}{\sqrt{2}} \begin{pmatrix} 1 & 1 \\ -i & i \end{pmatrix} \otimes I \tag{2.8}$$

where I is a $W \times W$ identity matrix, and defining $A_k \equiv -iUH(k)U^\dagger$, not to be confused with the vector potential, one can calculate the Majorana number [?] $\mathcal{M}$ of the 1D ribbon as [?]

$$\mathcal{M} = \text{sgn}\left[\text{Pf}(A_{k=0})\text{Pf}(A_{k=\pi})\right] \tag{2.9}$$

8

where Pf stands for the Pfaffian of a skew-symmetric matrix [?]. When $\mathcal{M} = -1$, the 1D system is in a nontrivial topological phase with MZM appearing at open ends of semi-infinite ribbons, and otherwise for $\mathcal{M} = 1$.

(a)

(b)
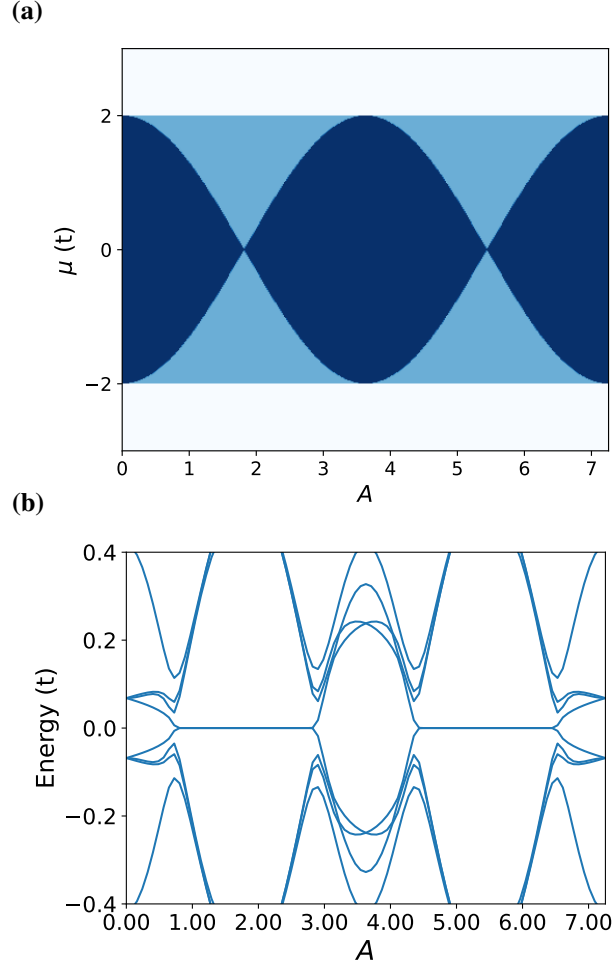
Figure 2.3: (a) Topological phase diagram for a $W = 1$ triangular chain with the Hamiltonian Eq. (2.7) obtained by superimposing the $\mathcal{M}(A, \mu)$ plots of 1D chains with $\mathbf{A} = A\hat{\mathbf{y}}$ and $\mathbf{A} = A(\frac{\sqrt{3}}{2}\hat{\mathbf{x}} + \frac{1}{2}\hat{\mathbf{y}})$. Color scheme: white—$\mathcal{M} = 1$, dark blue—$\mathcal{M} = -1$, light blue—$\mathcal{M} = 0$ (b) Near-gap BdG eigen-energies vs A for a finite triangle with edge length $L = 50$, $W = 1$, and $\mu = 1.6$.

In Fig. 2.3 (a) we show the topological phase diagrams for a 1D ribbon with width $W = 1$, $\mathbf{A} = A\hat{\mathbf{y}}$ and $\mathbf{A} = A(\frac{\sqrt{3}}{2}\hat{\mathbf{x}} + \frac{1}{2}\hat{\mathbf{y}})$ superimposed (see below). We found that the vector potential component normal to the ribbon length direction has no effect on the Majorana number, nor does the sign of its component along the ribbon length direction. However, topological phase transitions

can be induced by varying the size of the vector potential component along the ribbon, consistent with previous results [?, ?]. These properties motivate us to consider the structure of a hollow triangle formed by three finite-width ribbons subject to a uniform vector potential $\mathbf{A} = A\hat{\mathbf{y}}$ as illustrated in Fig. 2.1 (b). The light blue color on the phase diagram Fig. 2.3 (a) therefore means that the bottom edge and the two upper edges of the hollow triangle have different $\mathcal{M}$, which should give rise to MZM localized at the two bottom corners if the triangle is large enough so that bulk-edge correspondence holds, and gap closing does not occur at other places along its edges.

To show that corner MZM indeed appear when the conditions given by the phase diagram Fig. 2.3 (a) are met, we directly diagonalize the BdG Hamiltonian of a finite hollow triangle with edge length $L = 50$ and width $W = 1$. Fig. 2.3 (b) shows the spectral flow (BdG eigen-energies evolving with increasing vector potential A) close to zero energy at chemical potential $\mu = 1.6$. Indeed, zero-energy modes appear in the regions of μ and A consistent with the phase diagram (except when the bulk band gap is too small; see [?] for some examples.). Hollow triangles with larger larger W also have qualitatively similar behavior, although the phase diagrams are more complex [?]. The eigenfunctions for the zero-energy modes at $A = 2.75$ and $\mu = 1.6$ in Fig. 2.4 (b) also confirm their spatial localization at the bottom corners of the triangle.

We finally show that rotating the uniform vector potential in-plane can manipulate the positions of the MZM without hybridizing them with bulk states for certain ranges of μ and A. Fig. 2.4 (a) plots the spectral flow versus the in-plane azimuthal angle of $\mathbf{A}$, which clearly shows that the zero-energy modes persist throughout the rotation and the bulk gap never closes. Figs. 2.4 (b-d) plot the BdG wavefunctions of the MZM at special values of φ. One can see that the two MZM appear to cycle through the three vertices by following the rotation of $\mathbf{A}$. The robustness of the MZM therefore requires the condition of two edges being in a different topological phase from the third one to be satisfied throughout the rotation. Such a criterion combined with the individual phase diagrams of the edges can help isolate the desired parameter regions of μ and A. We also note that the positions of the MZM do not interchange after φ increases from 0 to π, different from the situation of the minimal Kitaev triangle in Fig. 2.2. The reason is that the MZM in the

(a)

(b) **(c)** **(d)**
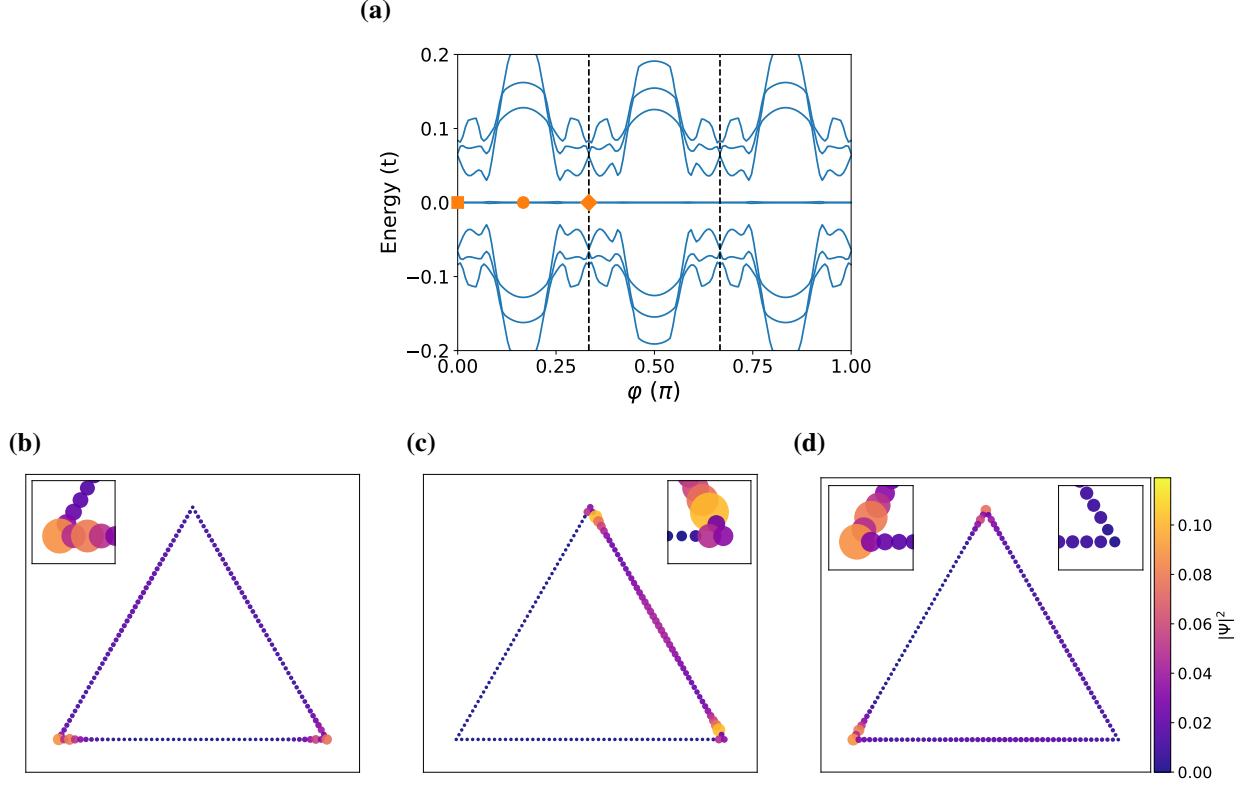
Figure 2.4: (a) Spectral flow of a hollow triangle with $W = 1$, $L = 50$, $\mu = 1.6$, and $A = 2.75$ with increasing rotation angle φ, defined through $\mathbf{A} = A(-\sin\varphi\hat{\mathbf{x}} + \cos\varphi\hat{\mathbf{y}})$. (b-d) BdG eigenfunction $|\Psi|^2$ summed over the two zero modes at $\varphi = 0$, $\frac{\pi}{6}$, and $\frac{\pi}{3}$, respectively.

latter case are not due to bulk-boundary correspondence [the values of $A = \frac{2\pi}{3\sqrt{3}}$ and $\mu = 0$ are a critical point in the phase diagram Fig. 2.3 (a)]. While the positions of the MZM at special points along the parameter path in the hollow triangle case have to be additionally constrained by the bulk topological phases of the three edges, that for the Kitaev triangle have more flexibility and are also protected by the finite size of the system.

A model that is closer to a realistic hollow triangular island is the finite-width triangular chain or ribbon. An example, illustrated in Figure 2.5 (c), has its edge length $L = 50$ and width $W = 3$. The phase diagram Fig. 2.5 (a) is created in a similar way as that in Fig. 2.3 (a), assuming a constant vector potential and infinitely long $W = 3$ ribbons. The spectral flow for the actual triangle with $\mu = 1.6$ in Fig. 2.5 (b) shows MZM in the parameter regions in agreement with the

11

(a)

(b)

(c)
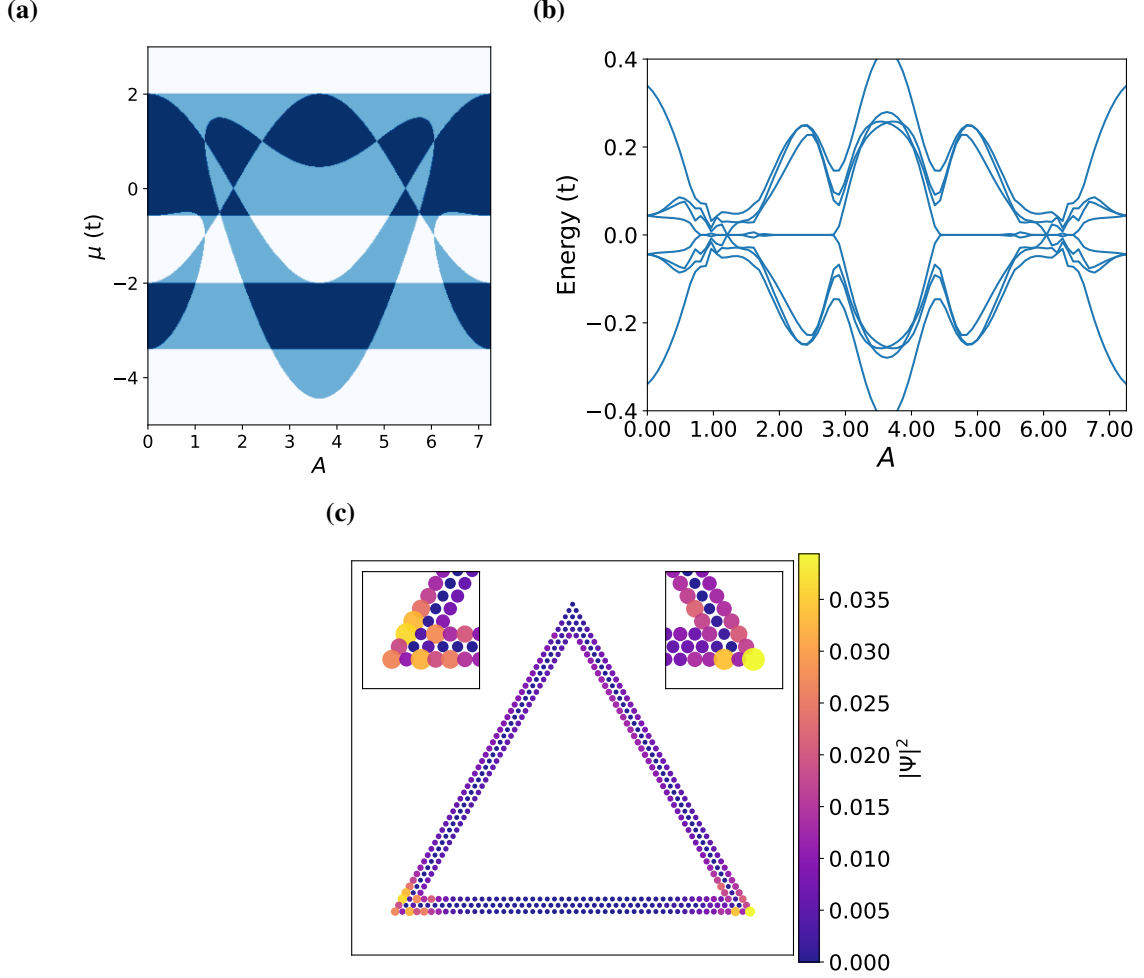
Figure 2.5: (a) Topological phase diagram for a $W = 3$ hollow triangle obtained by overlapping the $\mathcal{M}(A, \mu)$ plots of 1D chains with $\mathbf{A} = A\hat{\mathbf{y}}$ and $\mathbf{A} = A(\frac{\sqrt{3}}{2}\hat{\mathbf{x}} + \frac{1}{2}\hat{\mathbf{y}})$. Color scheme: white—$\mathcal{M} = 1$, dark blue—$\mathcal{M} = -1$, light blue—$\mathcal{M} = 0$ (b) Near-gap BdG eigen-energies vs A for a finite triangle with edge length $L = 50$, $W = 3$, and $\mu = 1.6$. (c) BdG eigenfunction $|\Psi|^2$ summed over the two zero modes at $A = 2.4709$.

phase diagram. Fig. 2.5 (c) plots the MZM wavefunction for $A = 2.7409$ and $\mu = 1.6$ that are indeed well localized at the bottom corners.

We next rotate the uniform vector potential to examine how the MZM move on a hollow triangle. Figure 2.6 shows the spectral flow and eigenfunctions as we rotate $\varphi = 0$ to $\varphi = \pi$ counterclockwisely. The two MZM cycle through the three vertices in a similar manner as that in Fig. 4 of the main text (only the MZM wavefunctions at $\varphi = 0$ and $\frac{\pi}{3}$ are plotted as representatives of the $\varphi = n\pi/3$ cases). Note that the spectral flow has 3-fold rotation symmetry but not 6-fold,
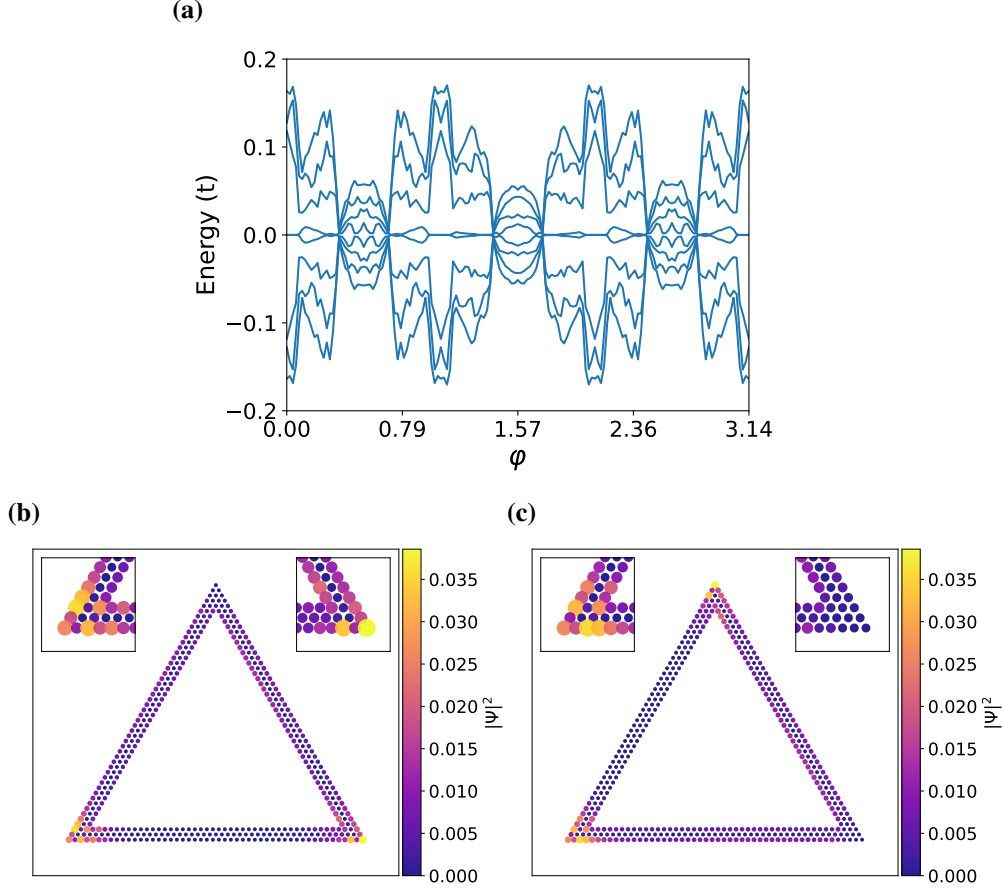
Figure 2.6: (a) Spectral flow of a hollow triangle with $W = 3$, $L = 50$, $\mu = 1.6$, and $A = 2.75$ with increasing rotation angle φ, defined through $\mathbf{A} = A(-\sin\varphi\hat{\mathbf{x}} + \cos\varphi\hat{\mathbf{y}})$. (b-c) BdG eigenfunction $|\Psi|^2$ summed over the two zero modes at $\varphi = 0$ and $\frac{\pi}{3}$, respectively.

since increasing φ by $\frac{2\pi}{3}$ is equivalent to rotating the coordinate system clockwisely by $\frac{2\pi}{3}$. In contrast, rotating the vector potential by $\frac{\pi}{3}$, if without an additional sign change of the p-wave pairing potential, is not an exact symmetry of the finite triangle. Also we did not try to scrutinize the phase diagram to find a parameter path in which the bulk gap does not close, as in the $W = 1$ case in the main text. Here we just point out that identifying a system-specific parameter path for adiabatic manipulation of MZM is in principle always possible, especially if one is allowed to have more knobs other than φ in real structures, such as tuning the chemical potential of individual edges or the size of the vector potential, etc.
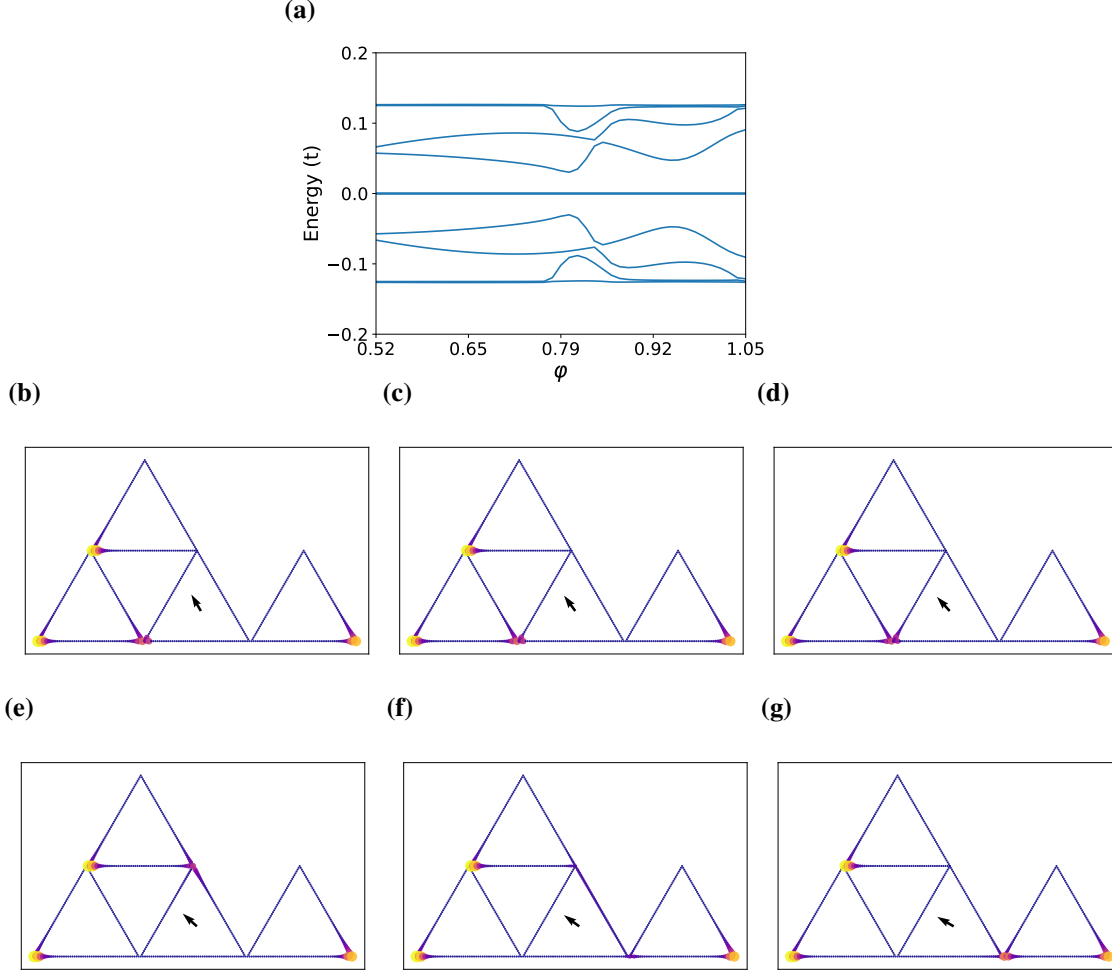
Figure 2.7: (a) Spectral flow for the critical step of swapping γ_2 and γ_3 in the example of Fig. 5 in the main text, calculated using four corner-sharing triangles of $W = 1$ and $L = 50$, with $\mu = 1.6$ and $A = 2.6$. Vector potential for the middle triangle in the bottom row can rotate according to $\mathbf{A} = A(-\sin\varphi\hat{\mathbf{x}} + \cos\varphi\hat{\mathbf{y}})$ from $\varphi = \frac{\pi}{6}$ to $\frac{\pi}{3}$, while the other three have fixed $\varphi = 0$. (b)-(g) BdG eigenfunction $|\Psi|^2$ summed over the four zero modes at equally-spaced points along the rotation path. The black arrow indicates the direction of the vector potential for the bottom middle triangle.

2.4 Braiding MZM in a small network of triangles

In this section we show that one can braid two out of four MZM, a minimal setting for nontrivial manipulation of the degenerate many-body ground states, by using a small network of corner-sharing triangles. We focus on the critical step of swapping γ_2 and γ_3 as labeled in Fig. 5 of the main text. This can be done by rotating the vector potential of the triangle in the middle of the bottom row from $\varphi = \frac{\pi}{6}$ to $\frac{\pi}{3}$. More specifically, when $\varphi = \frac{\pi}{6}$, with the chosen values of μ and A, only the right edge of the said triangle is topologically nontrivial. The chain that hosts $\gamma_{3,4}$ thus

14

extends through this nontrivial edge to the top triangle as in Fig. 2.7 (b). On the other hand, when φ increases to $\frac{\pi}{3}$, the nontrivial edge of the middle triangle changes from right to left, which leads to γ_2 hopping from its left corner to the right through the top corner, while γ_3 is unaffected [Figs. 2.7 (c-g)]. As a result the γ_2, γ_3 swapping is done without closing the bulk gap, as can be seen from the spectral flow in Fig. 2.7 (a).

2.5   Additional results using inhomogeneous vector fields

While we have showed a constant vector field works to induce and manipulate MZM for a triangular chain and hollow triangle it remains to be seen if inhomogeneous vector potential fields can repoduce the same results. We expect this to be the case due to the topological phase diagram seen in 2.3 (a) and 2.5 (a) and the results that followed for a constant vector potential.

(a)   (b)
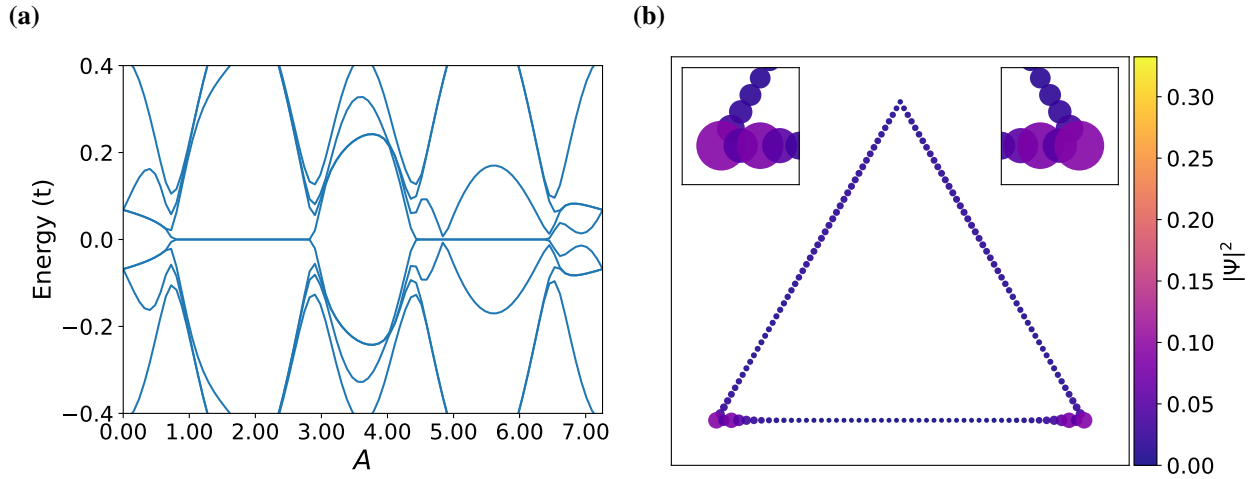
Figure 2.8: (a) Spectral flow of a hollow triangle with $W = 1$, $L = 50$, and $\mu = 1.6$ for increasing heaviside vector potential strength defined by $\mathbf{A} = A[1 - 2\Theta(x)]\hat{\mathbf{y}}$ (b) BdG eigenfunction $|\Psi|^2$ summed over the two zero modes at $A = 2.7409$.

For hollow triangle of width, $W = 1$ subject to a heaviside vector potential we see a similar spectral flow and MZM in Fig. 2.8 to match 2.3. If the heaviside vector potential is not so easily made in lab it may be easier to model a tanh function instead. Also, in the limit that the tanh's function width, w, goes to zero it is equivalent to the heaviside function. A tanh vector potential

15

(a)

(b)
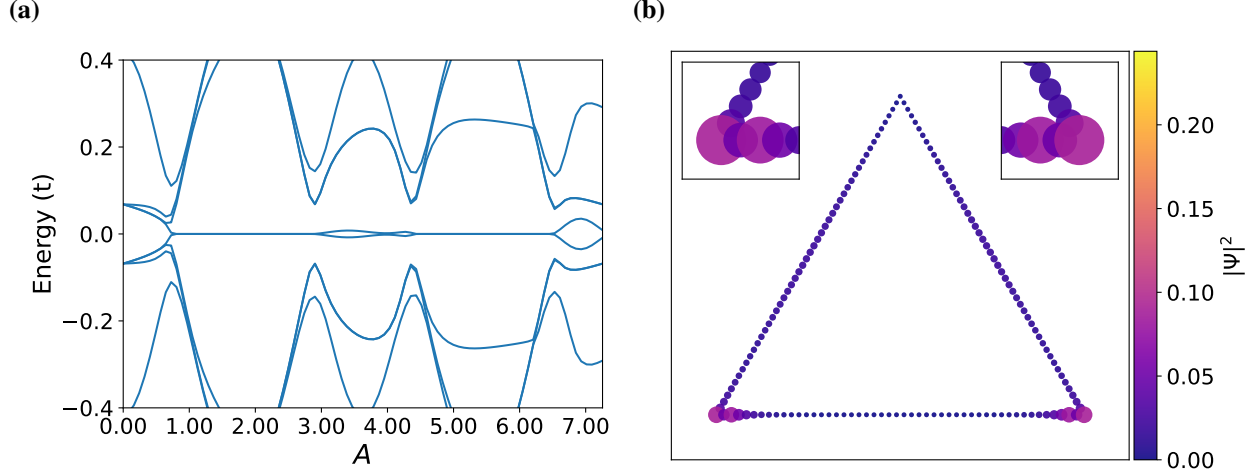
Figure 2.9: (a) Spectral flow of a hollow triangle with $W = 1$, $L = 50$, and $\mu = 1.6$ for increasing tanh vector potential strength defined by $\mathbf{A} = -A \tanh(x/2w)\hat{\mathbf{y}}$, $w = a/2$ (b) BdG eigenfunction $|\Psi|^2$ summed over the two zero modes at $A = 2.7409$.

can match the same results as seen in Fig. 2.9. It should be mentioned that the width of the tanh function should be on the order or smaller than the distance between to neighboring lattice points, if two neighboring sites overall phase accumulation is not large enough to match the topological phase diagram then the bulk edge correspondence at the tanh's inflection point would cause additional MZM to appear. In other words, the top edges of the triangle should be one long bent trivial edge but if the tanh's width is too large the two edges become separated by a small non-trivial topological corner-edge because the Peierls phase is too small. Increasing the width of the hollow triangle to $W = 3$, we see similar results for heaviside, Fig. 2.10, and tanh, Fig. 2.11, compared to a constant vector potnential, Fig. 2.5.

We look at a linear vector potential next. A topological phase diagram for a linear vector potential is possible to compute, however, it requires a lattice space matrix instead of momentum space matrix due to having no periodic boundary conditions. It also requires separate calculations for longer traingular lattice ribbons. Computation times can become unruly when modeling large triangles for a high density phase diagram of A and μ values. We could, however, use the topological phase diagram in Fig. 2.3 to guess the topology for the varying Peierls phases along an edge. Fig. 2.12 shows some critical points for MZMs to appear with $\mu = 0$ for a hollow triangle of

(a)

(b)

Figure 2.10: (a) Spectral flow of a hollow triangle with $W = 3$, $L = 50$, and $\mu = 1.6$ for increasing heaviside vector potential strength defined by $\mathbf{A} = A[1 - 2\Theta(x)]\hat{\mathbf{y}}$ (b) BdG eigenfunction $|\Psi|^2$ summed over the two zero modes at $A = 2.7409$.

(a)

(b)

Figure 2.11: (a) Spectral flow of a hollow triangle with $W = 3$, $L = 50$, and $\mu = 1.6$ for increasing tanh vector potential strength defined by $\mathbf{A} = -A\tanh(x/2w)\hat{\mathbf{y}}$, $w = a/2$ (b) BdG eigenfunction $|\Psi|^2$ summed over the two zero modes at $A = 2.7409$.

$W = 1$ and $W = 3$, respectively. Fig. 2.13 shows apparent zero modes for a range of A values for a hollow triangle of $W = 1$ and $W = 3$, respectively. For similar reasons why the tanh function width needs to be small, it may be difficult to have the upper parts of the triangles top edges be all trivial topology, a small section may centered on the top corner may be non-trivial, thus hosting additional MZMs, as seen in Fig. 2.13 (c-d) half way up the triangles.
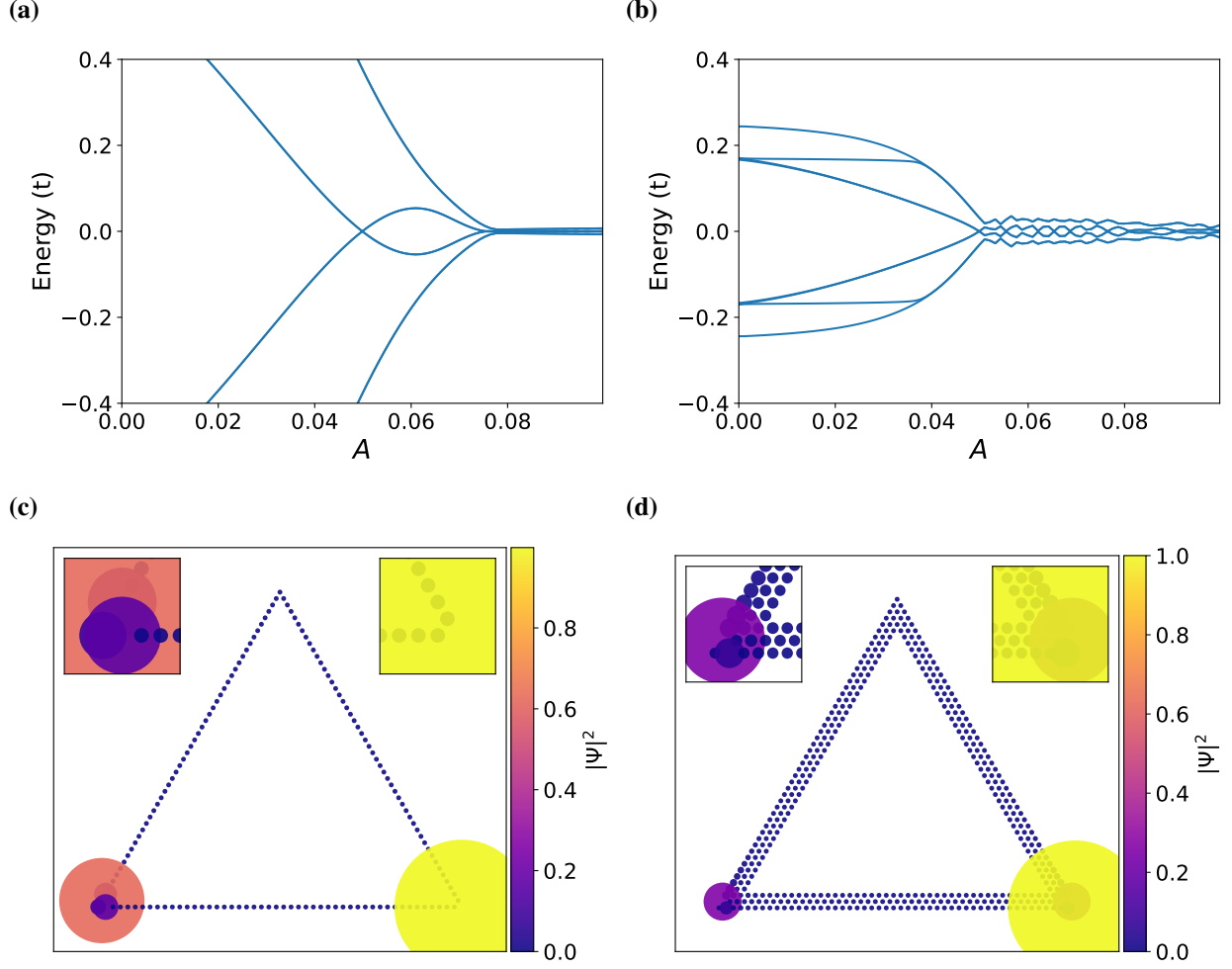
Figure 2.12: Spectral flow of a hollow triangle with $L = 50$, and $\mu = 0$ for increasing linear vector potential strength defined by $\mathbf{A} = -Ax\hat{\mathbf{y}}$ (a) $W = 1$ and (b) $W = 3$ (c-d) Wavefunctions of the MZM at $A = 0.0499$ for both widths, respectively.

2.6 Discussion

The hollow interior of the triangles considered in this work is needed for two reasons: (1) $W \ll L$ is required for bulk-edge correspondence based on 1D topology to hold; (2) A finite W is needed to gap out the chiral edge states of a 2D spinless p-wave superconductor based on which Eq. (2.7) is written. The latter is not essential if one does not start with a spinless p-wave supercondutor but a more realistic model such as the Rashba+Zeeman+s-wave pairing model. On the other hand, the former constraint may also be removed if one uses the Kitaev triangle. Nonetheless, an effective 3-site Kitaev triangle may emerge as the effective theory of triangular
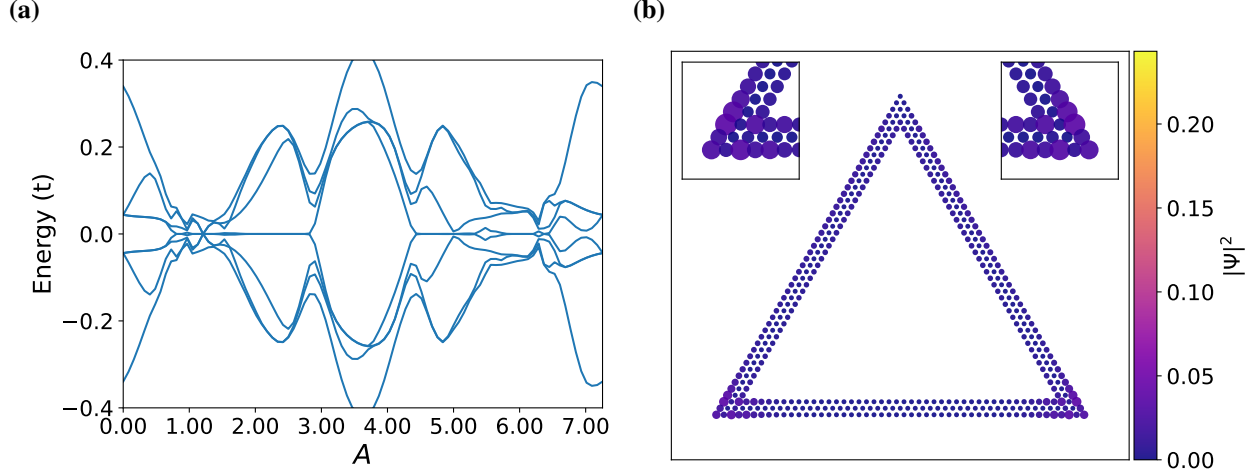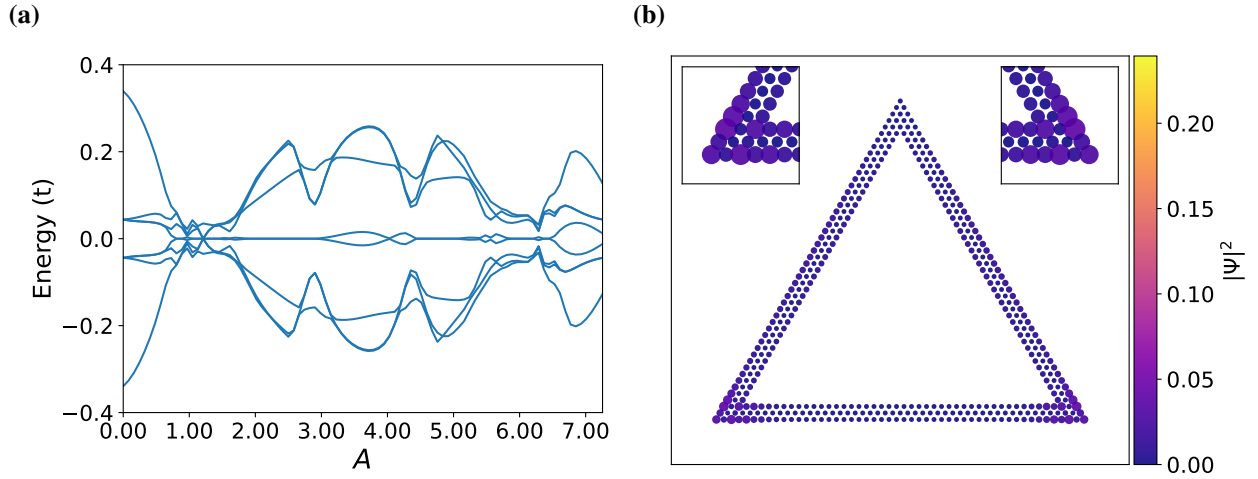
18

(a)

(b)

(c)

(d)
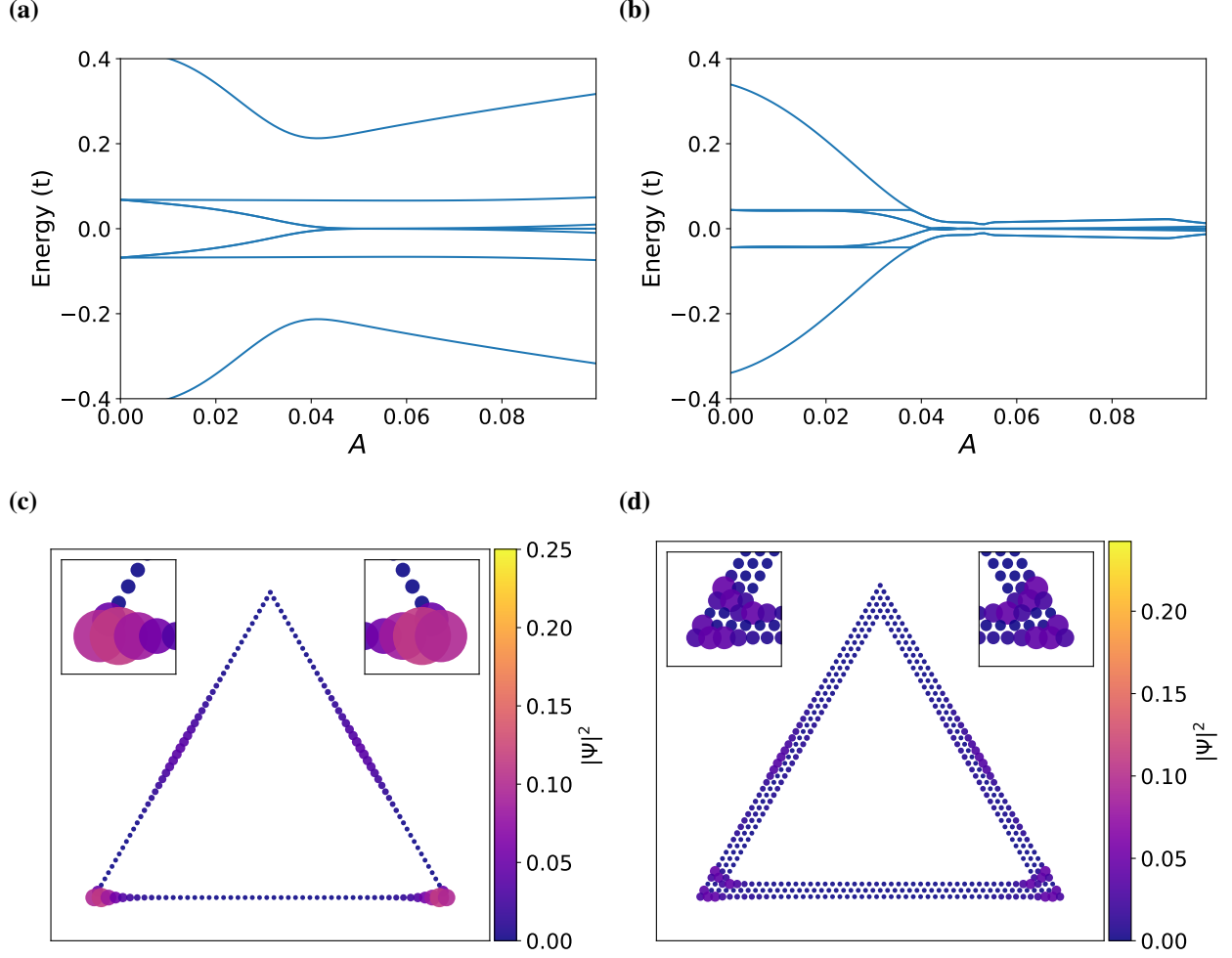
Figure 2.13: Spectral flow of a hollow triangle with $L = 50$, and $\mu = 1.6$ for increasing linear vector potential strength defined by $\mathbf{A} = -Ax\hat{\mathbf{y}}$ (a) $W = 1$ and (b) $W = 3$. (c-d) Wavefunctions of the MZM at $A = 0.0598$ for both widths, respectively.

structures if a three-orbital low-energy Wannier basis can be isolated, similar to the continuum theory of moiré structures. We also note in passing that the corner MZM in our triangles appear due to different reasons from that in higher-order topological superconductors [**?, ?**].

For possible physical realizations of our triangles, immediate choices are quantum dots forming a Kitaev triangle [**?**], planar Josephson junctions or cuts on quantum anomalous Hall insulator/superconductor heterostructures [**?**] that form a hollow triangle, and triangular atomic chains assembled by an STM tip [**?**] on a close-packed surface. The quantum-dot platform may be advantageous in the convenience of implementing parity readout by turning the third vertex temporarily

into a normal quantum dot [?, ?, ?]. Looking into the future, it is more intriguing to utilize the spontaneously formed triangular islands in epitaxial growth [?] with the center region removed either physically by lithography/ablation, or electrically by gating. To create a staggered vector potential or supercurrent profile for the Kitaev triangle, one can use a uniform magnetic field, corresponding to a constant vector potential gradient, plus a uniform supercurrent that controls the position of the zero. It is also possible to use two parallel superconducting wires with counter-propagating supercurrents proximate to the triangle.
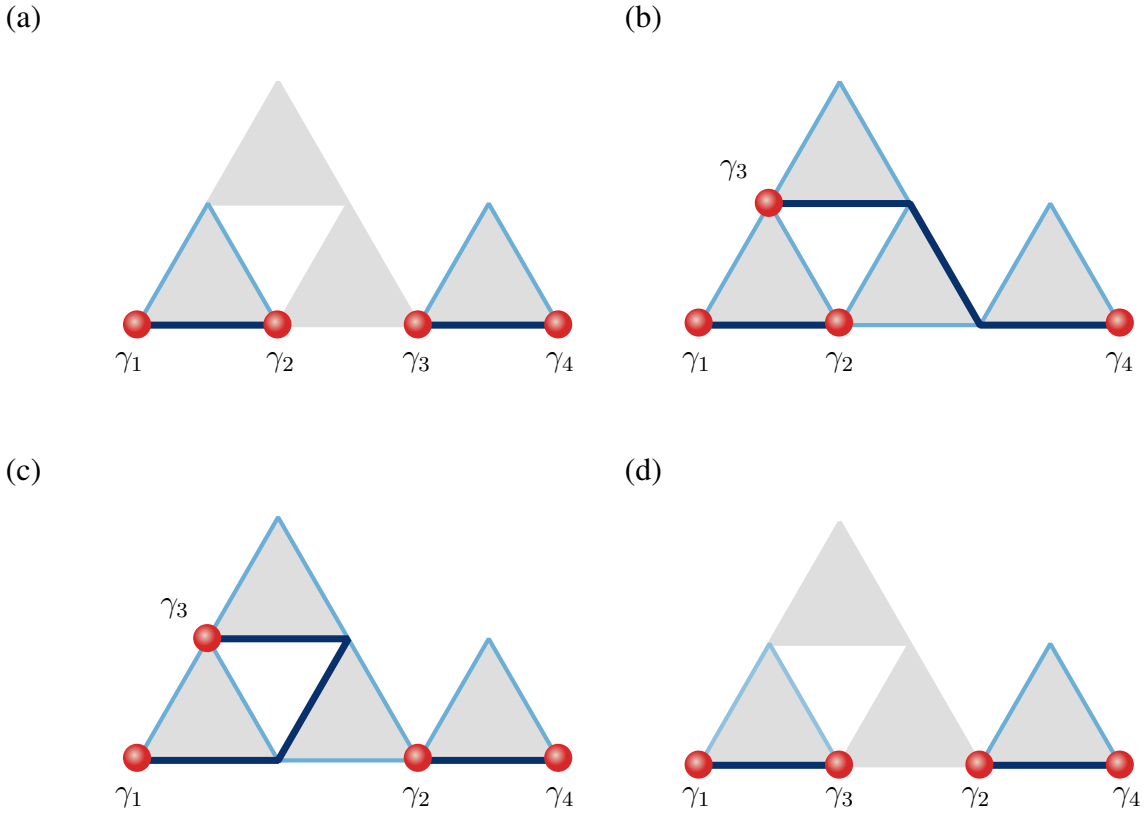
Figure 2.14: Representative steps for braiding four MZM in four triangles sharing corners. (a) Initialization of four MZM $\gamma_1, \gamma_2, \gamma_3, \gamma_4$. All three edges of the bottom-middle and the top triangles are in the trivial phase by e.g. controlling the chemical potential. The bottom-left and bottom-right triangles have $\varphi = 0$ so that their bottom edges are nontrivial. (b) Moving γ_3 by "switching on" the middle triangle by changing the chemical potential under a fixed vector potential at $\varphi = \frac{\pi}{6}$, and then turning on the top triangle with similar means except $\varphi = 0$. (c) Transporting γ_2 to the right triangle through rotating the vector potential in the middle triangle counterclockwise by $\pi/6$. (d) Moving γ_3 to the left triangle by "switching off" the top triangle followed by the middle triangle.

A tentative design for braiding more than two MZM, illustrated in Fig. 2.14, consists of four triangles sharing corners with their neighbors. The critical step of transporting γ_2 to the left vertex of the rightmost triangle, corresponding to Figs. 2.14 (b,c), can be achieved by rotating the vector potential of the bottom-middle triangle counterclockwisely from $\varphi = \frac{\pi}{6}$ to $\frac{\pi}{3}$, which swaps the topological phases of the two side edges as shown in Fig. 2.4. In [**?**] we show this operation does not involve gap closing at least for certain parameter regions. Our work provides a versatile platform for manipulating MZM based on currently available candidate MZM systems and for potentially demonstrating the non-Abelian nature of MZM in near-term devices.

Chapter 3

Floquet Landau Levels

1. Introduction (Tahir's intro is fine, maybe in my own words, Floquet engineering)

    i Time dependent, motivation—QAHE gap but not QHE gap

    ii Floquet Theorem— quasi-energy spectrum

2. Results

    i square + A(t) (Tahir's perturbative calc)

    ii honeycomb + A(t) (Tahir's perturbative calc)

3. Discussion and future

3.1 Introduction

The quantum Hall effect (QHE) in conventional two-dimensional electron gas (2DEG) is one of the most remarkable phenomena in condensed matter physics [**?**]. This effect is indeed associated with a uniform external perpendicular magnetic field, which splits the electron energy spectrum into discrete Landau levels (LLs). Subject to a strong magnetic field, the diagonal (longitudinal) electric conductivity is vanishingly small, while the nondiagonal (Hall) conductivity is quantized. This happens due to the fact that, when the Fermi energy lies in the gap between two LLs, it is referred to as integer QHE as the Hall conductivity takes values of $2(n+1)e^2/h$ with an integer n. Recent experimental realization of graphene has stimulated additional interest to explore QHE in two dimensional systems [**?**,**?**,**?**]. Graphene exhibits unusual quantized Hall conductivity values of $2(2n+1)e^2/h$ due to application of the magnetic field [**?**], which are different from conventional 2DEG.

This significant effect is important to explore in Floquet systems [**?**,**?**] because one may want to observe new phases in an alternative venue that can be experimentally realized [**?**,**?**,**?**,**?**].

Time periodically modulated Floquet theory has been extensively studied and well established for a large class of systems [?, ?, ?, ?, ?, ?]. Therefore, one may employ the high frequency expansions [?, ?, ?, ?, ?, ?, ?, ?, ?] such as the well known Floquet-Magnus expansion [?, ?, ?, ?] and Van Vleck expansion [?, ?]. The significant difference is that latter provides an explicit formulas for the time evolution operator starting at initial time $t_0 = 0$ rather than former starting with finite time t_0 [?]. In such nonequilibrium systems, a circularly polarized laser light made topology nontrivial in spite of triviality in equilibrium [?]. This nontrivial topology is similar to the quantum Anomalous Hall effect proposed by Haldane [?]. Further, optical manipulation of matter is emerging as a promising way of exploring novel phases [?, ?]. This leads to Floquet-Bloch states exhibiting emerging physical properties that are otherwise inaccessible in equilibrium [?], i.e., the Floquet Chern insulator [?], Floquet notion of magnetic and other strongly-correlated phases [?], topological classifications, symmetry-breaking concept, and symmetry protected topological phases in nonequilibrium quantum many-body systems [?, ?]. Furthermore, it is important to note that these studies have been demonstrated in the presence of time-periodic homogeneous laser lights. However, the application of spatially inhomogeneous [?, ?, ?, ?, ?] laser lights have not been considered so far to best of our knowledge.

In this Letter, it is stirring to unveil that QHE can be observed in Floquet systems without need of uniform magnetic field. We show that two linearly polarized lights are an effective and versatile way of realizing QHE either in graphene-like 2D systems or in conventional 2DEG. Additionally, any one or both lights need to be spatially inhomogeneous. Employing the Floquet theory, we rely on the standard degenerate perturbation formalism and use the Van Vleck expansion [?, ?, ?]. Finally, to obtain the effective Hamiltonian and corresponding bandstructure, we employ the long wavelength limit for spatially inhomogeneous modulation. We believe that our work provides a new platforms for realizing QHE and related novel phases in nonequilibrium systems.

3.2 Floquet LLs in Dirac systems

Dirac electrons can be represented with a generic model Hamiltonian like 2D graphene monolayer,

$$H^D = v_F(\sigma_x \Pi_x + \sigma_y \Pi_y), \tag{3.1}$$

where $\mathbf{\Pi} = \mathbf{p} + e\mathbf{A^D}$, here $\mathbf{A^D}$ is the vector potential, $\mathbf{p}$ is the momentum operator, v_F is the Fermi velocity of Dirac fermions, e the absolute value of electron charge, and σ the Pauli matrices vector in 2D. We have two linearly polarized laser lights with the electric field components

$$\mathbf{E}_1 = E\cos(\omega t)\hat{\mathbf{x}}, \mathbf{E}_2 = E\sin(Kx)\sin(2\omega t)\hat{\mathbf{y}}, \tag{3.2}$$

where second light is spatially inhomogeneous. It is important to note that second light need to have twice higher frequency than first. This is basic requirement to have LLs spectrum in Dirac systems. Further, one light is propagating along y-axis and polarization is along x-axis, and the other is propagating along x-axis and polarization along y-axis. The ω is frequency of light with time t, $K = 2\pi/a$ with a being the spatial period of the electric field with amplitude E. This form of the field leads ($\mathbf{E} = -\frac{\partial \mathbf{A^D}}{\partial t}$) to the following vector potential $\mathbf{A^D}$

$$\mathbf{A^D} = (-V_y \sin(\omega t), V_x \cos(2\omega t), 0), \tag{3.3}$$

where we have $V_y = \frac{ev_F E}{\omega}, V_x = \frac{ev_F E}{2\omega}\sin(Kx)$. Substituting Eq. (3.3) into Eq. (3.1), we arrive at

$$H^D(t) = H_0^D - \sigma_x V_y \sin(\omega t) + \sigma_y V_x \cos 2(\omega t), \tag{3.4}$$

where $H_0^D = v_F(\sigma_x p_x + \sigma_y p_y)$. Because of the time-translation symmetry through $A(t + T) = A(t)$ with $T = 2\pi/\omega$, one can apply the Floquet theory [?, ?, ?] and obtain an effective Hamiltonian from Eq. (3.4). After performing the Fourier transform of the time-periodicity, first and second order expansion in $\hbar\omega$ terms leads to the final effective Hamiltonian in

Eq. (3.4) as

$$H_{\text{eff}}^D = H_0^D - \frac{V_y^2 v_F \sigma_y p_y}{\hbar^2 \omega^2} - \frac{V_y^2 V_x \sigma_y}{2\hbar^2 \omega^2} - \frac{v_F \sigma_x (V_x^2 p_x + p_x V_x^2)}{8\hbar^2 \omega^2}. \tag{3.5}$$

In Eq. (3.5), first order term in $\hbar\omega$ that leads to gap at the Dirac point in usual circularly polarized light experiments [?, ?] is zero here due to inhomogeneous nature of laser lights. This effective Hamiltonian can be simplified in the long wavelength limit to

$$H_{\text{eff}}^D = v_F' \sigma_x p_x + v_F \sigma_y (p_y - eB^D x) \tag{3.6}$$

In obtaining Eq. (3.6), last term in Eq. (3.5) is second order in space and thus zero in the long wavelength limit for the spatially inhomogeneous modulation. Further, we have $v_F' = v_F/C$, $B^D = \frac{V_y^2 E}{4\hbar^2 \omega^3 C} K$, with $C = 1 - V_y^2/(\hbar^2 \omega^2)$. In accordance with Eqs. (3.5) and (3.6), there is least anisotropy in the Dirac spectrum in addition to zero gap. Diagonalizing the Hamiltonian in Eq. (3.6), we obtained the eigenvalues for Dirac system as

$$E_n^D = \sqrt{n(v_F' v_F B^D) 2e\hbar}, \tag{3.7}$$

which is similar to graphene LLs spectrum in the limit of equal velocities. We can have gapped Dirac spectrum by using uniform circularly polarized laser light as observed in experiments [?, ?] or by using any substrate like hBN. It is also important to note that the effective magnetic field strength obtained for Dirac case in Eq. (3.7) is directly proportional to third order of the electric field and inversely proportional to the product of spatial period and fifth order of the frequency of the polarized light $\propto (E^3/(a\omega^5))$. This factor of the laser lights can be tuned and thus effective magnetic field can be enhanced in such nonequilibrium situations.
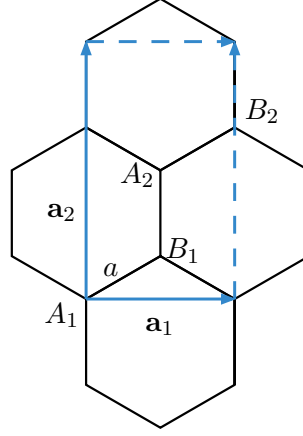
3.2.1 Dirac Numerical Approach

We now look beyond perturbation theory. In doing so we will have to solve the system numerically, which we will describe next. The incident laser light doesn't allow for translation symmetry along the x-axis for our Dirac honeycomb system. We consider a simple model using 4 atoms in a unit cell, the lattice vectors are $\mathbf{a}_1 = \sqrt{3}a\hat{\mathbf{x}}$ and $\mathbf{a}_2 = 3a\hat{\mathbf{y}}$, as can be seen in figure **??**. Our Hamiltonian takes the following form

$$H = -\sum_{j'l'\alpha, jl\beta} t_{jl\beta}^{j'l'\alpha} C_{j'l'\alpha}^{\dagger} C_{jl\beta} + h.c., \tag{3.8}$$

where t is the hopping amplitude, j, l are unit cell index in x and y, and $\alpha, \beta = A_1, A_2, B_1, B_2$. The vector potential is

$$\mathbf{A}(\mathbf{r}, t) = -\frac{E}{\omega}\sin(\omega t)\hat{\mathbf{x}} + \frac{E}{2\omega}\sin(Kx)\cos(2\omega t)\hat{\mathbf{y}}. \tag{3.9}$$

To include the vector potential in the tight-binding model we consider a finite system defined by $r_c \geq \max(|x_{i\alpha}|, |y_{i\beta}|)$. Using a Peierls substitution we can write the hopping term as

$$t_{jl\beta}^{j'l'\alpha} = \exp\left[i\phi_0 \left\{ (x_{j'l'}^{\alpha} - x_{jl}^{\beta})\sin\omega t - \frac{1}{2}\sin\left(K\frac{x_{j'l'}^{\alpha} + x_{jl}^{\beta}}{2}\right)(y_{j'l'}^{\alpha} - y_{jl}^{\beta})\cos 2\omega t \right\}\right]$$

$= \exp\left[iX_1\sin(\omega t) - iX_2\cos(2\omega t)\right]$ where $t = 1$ and $\phi_0 = \frac{eEa}{\hbar\omega}$. One can fourier transform

along the y-axis to momentum space to simplify our system to

$$H = -\sum_{jk} \left[\Psi_{jk}^\dagger H_{j,j} \Psi_{jk} + \Psi_{j+1,k}^\dagger H_{j+1,j,k}' \Psi_{jk} + h.c. \right], \tag{3.10}$$

where $\Psi_{jk} = [C_{jkA_1}, C_{jkB_1}, C_{jkA_2}, C_{jkB_2}]^T$. The two matrices are

$$H_{j,j} = \begin{bmatrix} 0 & t_{jlB_1}^{jlA_1} & 0 & 0 \\ t_{jlA_1}^{jlB_1} & 0 & t_{jlA_2}^{jlB_1} & 0 \\ 0 & t_{jlB_1}^{jlA_2} & 0 & t_{jlB_2}^{jlA_2} \\ 0 & 0 & t_{jlA_2}^{jlB_2} & 0 \end{bmatrix}$$

and

$$H_{j+1,j,k}' = \begin{bmatrix} 0 & t_{jlB_1}^{j+1,lA_1} & 0 & t_{jlB_2}^{j+1,l+1,A_1} e^{i\mathbf{k}\cdot\mathbf{a}_2} \\ 0 & 0 & 0 & 0 \\ 0 & 0 & 0 & t_{jlB_2}^{j+1,lA_2} \\ 0 & 0 & 0 & 0 \end{bmatrix},$$

where $\mathbf{k} = k\hat{\mathbf{y}}$. The Hamiltonians dimension is reduced to $N_S \times N_S$, with $N_S = 2r_c + 1$.

For Floquet theorem we next consider how to construct the Quasienergy operator $\bar{Q}$. We first need to calculate the fourier time transform of our Hamiltonian. Each component of the matrix can be written as the following

$$H_{ab,n} = \frac{1}{T} \int_0^T H_{ab} e^{-in\omega t} dt$$

$$= \frac{1}{2\pi} \int_0^{2\pi} e^{iX_1 \sin(\tau) - iX_2 \cos(2\tau) - in\tau} d\tau. \tag{3.11}$$

This integral form is close to a Bessel function but has no elementary solution and we solve it numerically. The quasienergy matrix $\bar{Q}$ then has matrix elements

$$\bar{Q}_{m,m+n} = H_n - m\hbar\omega\delta_{n0} \tag{3.12}$$

27

We choose a cutoff for mode m, $|m| \leq m_c$, where m_c is a positive integer. This means we will have $N_m = 2m_c + 1$ diagonal blocks, where each block is a $N_S \times N_S$ matrix, H_n.

3.3 Floquet LLs in 2DEG

Next, similar to Dirac electrons, we consider the case of Schrödinger electrons under the application of two linearly polarized laser lights. The unperturbed Hamiltonian for 2DEG is

$$H = \frac{\pi_x^2}{2m^*} + \frac{\pi_y^2}{2m^*}, \tag{3.13}$$

where m^* is the effective mass of electron. By changing the Hamiltonian into a time-dependent form by applying two linearly polarized lights such that $\pi \to \mathbf{p} - \mathbf{eA(t)}$. Therefore, Eq. (3.13) is written as

$$H(t) = \frac{1}{2m^*}[p_x + eA_x(t)]^2 + \frac{1}{2m^*}[p_y + eA_y(t)]^2, \tag{3.14}$$

where the electric field components for two spatially inhomogeneous linearly polarized laser lights are

$$\mathbf{E}_1 = E\cos(\omega t)\hat{\mathbf{x}}, \mathbf{E}_2' = E\cos(Kx)\sin(\omega t)\hat{\mathbf{y}}. \tag{3.15}$$

It is important to note that second electric field in Eq. (3.15) is different from similar field used for Dirac spectrum given in Eq. (3.2). This is due to the fact that Schrödinger Hamiltonian is quadratic rather than linear as in case of Dirac electrons. This is basic requirement for the Schrödinger electron spectrum to exhibit LLs. The field give in Eq. (3.15) lead to the following vector potential $\mathbf{A}(t)$

$$\mathbf{A}(t) = (-V_1\sin(\omega t), V_2\cos(\omega t), 0), \tag{3.16}$$

where we have $V_1 = \frac{eE}{\omega}, V_2 = V_1 \cos(Kx)$. Employing the Floquet theory similar to Dirac electrons, we obtain the effective Hamiltonian as

$$H_{\text{eff}} = H_0 - \frac{U}{m^*}\sin(Kx)p_y - \frac{U^2}{4m^*}V_1^2 \cos(2Kx). \quad (3.17)$$

For Landau Level problem, we usually use the Landau gauge with vector potential like $A = (0, xB, 0), B = B\hat{\mathbf{z}}$. In the long wavelength limit, Eq. (3.17) can be simplified to

$$H_{\text{eff}} = \frac{p_x^2}{2m^*} + \frac{1}{2m^*}[p_y + eBx]^2 - \frac{U^2}{4m^*}, \quad (3.18)$$

where $U = \frac{KV_1^2}{2m^*\omega}$, and the effective magnetic field $B = \frac{K^2V_1^2}{em^*\omega}$. Eq. (3.18) is a standard LL problem in the presence of an external perpendicular magnetic field. Therefore, by diagonalizing the effective Hamiltonian, the corresponding energy eigenvalues are obtained as

$$E_n = (n + \frac{1}{2})\hbar\omega_c - \frac{U^2}{4m^*}, \quad (3.19)$$

where $\omega_c = \frac{eB}{m^*}$. We can see from Eq. (3.19) that the effective magnetic field is directly proportional to the strength of the electric field (second order) and inversely proportional to the product of second order spatial period and third order of the frequency of the laser lights $\propto (E^2/(a^2\omega^3))$. This factor of the lase lights can be tuned to enhance the strength of the effective magnetic field in nonequilibrium systems.

3.4 Discussion and conclusion

Results can be explained with the help of existing experiments [?, ?] and can provide an estimate for the strength of the effective magnetic field to observe LLs and QHE. Analytical structure of Eq. (3.7) and Eq. (3.19) is primarily responsible for the LLs spectrum in both the Dirac and Schrödinger systems, respectively. Although such results are valid for other 2D materials or Schrödinger systems, however, for simplicity, we will consider parameters

realized for graphene or topological insulators [**?**, **?**]. In these experiments [**?**, **?**], the strength of the electric field used is 1×10^7 V/m to 1×10^8 V/m and the frequency of the light varies from 120 meV to 191 meV.

In case of Dirac electrons, we calculate the effective magnetic field strength using Eq. (3.7). For a fixed value of the spatial period of 120 nm and frequency of laser light $\hbar\omega = 191$ meV, the strength of the effective magnetic field is $\approx$ 10 Tesla for electric field strength of 5×10^7 V/m [**?**]. Moreover, by reducing the spatial period to 12 nm, we obtain the effective magnetic field $\approx$ 98 Tesla for fixed frequency ($\hbar\omega = 191$ meV) and electric field (5×10^7 V/m). This is due to the fact that effective magnetic field is directly proportional to electric field and inversely proportional to the spatial period of light according to Eq. (3.7). Similarly, keeping the spatial period constant and increasing the electric field strength, we can increase the strength of the effective magnetic field for larger frequencies only. However, for the frequency $\hbar\omega = 191$ meV, we can not go beyond 5×10^7 V/m value of the electric field irrespective of the spatial period. This limitation is due to the factor "C" in Eq. (3.7). Further, using lower light frequency ($\hbar\omega = 120$ meV) as realized in topological insulators experiments [**?**], the critical strength of the electric field is 2×10^7 V/m beyond which magnetic field will become negative. Additionally, for larger frequency of 220 meV, the maximum value of electric field 7×10^7 V/m can be used. It is also important and interesting to note that negative values of the effective magnetic field at larger strengths of light's electric field are fruitful. This is because positive or negative values of the effective magnetic field means (see Eq. (3.6)) that magnetic field is applied either from positive z-axis or negative z-axis. **This estimate of parameters is equally valid for frequency space expansion results (Fig. 1) obtained numerically and degenerate perturbation (Fig. 2) analysis.**

In case of Schrödinger electrons in conventional 2DEG systems, the effective magnetic field strength can be obtained using Eq. (3.19). For a fixed value of the spatial period of 100 nm and light frequency of $\hbar\omega = 191$ meV, the strength of the effective magnetic field is 1 Tesla using electric field of 5×10^7 V/m. Further, by reducing the spatial period to 10

nm and keeping the electric field (5×10^7 V/m) and frequency of light ($\hbar\omega = 191$ meV) fixed, we obtain the effective magnetic field ≈ 106 Tesla. This can be understood from Eq. (3.19). In contrast to Dirac case, by increasing the strength of electric field of light, we can increase the strength of the effective magnetic field values. For example, for fixed period of 100 nm and frequency ($\hbar\omega = 191$ meV), the effective magnetic field is 17 Tesla for 2×10^8 V/m. Next, we see the impact of increasing or decreasing frequency and keeping period (100 nm) and electric field (5×10^7 V/m) fixed. For decreasing frequency to 120 meV, we obtain larger effective magnetic field (4.3 Tesla) while increasing frequency leads to smaller effective magnetic field (0.7 Tesla at 220 meV light frequency). **This estimate of parameters is equally valid for frequency space expansion results (Fig. 1) obtained numerically and degenerate perturbation (Fig. 2) analysis.**

In conclusion, we have shown Floquet LLs and the QHE using two linearly polarized lights for graphene-like 2D and conventional 2DEG systems. While using these laser lights, we need at least one or both polarized lights to be spatially inhomogeneous. We have presented results using frequency space expansion method, degenerate Floquet perturbation theory, tight binding models and numerical model calculations. All the results are agreed well to show Floquet LLs in experimentally accessible parameters range. Also, it is interesting to note that we are flexible to use different values of the electric field strength, frequency or spatial period of the light to realize QHE and control the strength of the effective magnetic field. Therefore, we believe that Floquet LLs and QHE can be observed in the experiments for moderate strength of the spatially inhomogeneous lights **as shown in Figs. 1 and 2.** Moreover, we expect the potential to host new nano-electronics in nonequilibrium systems.

Bibliography

Chapter 4

Conclusion and Discussion

What makes gauge potential unique in creating/tuning/manipulating new topoglical systems

Applications

Appendix A

Suitable Name

1. Majorana Number derivation

2. Other derivations not included in introduction

A.1 Kitaev Triangle and Peierls substitution

We start with a spinless or spin-polarized p-wave superconductor

$$\mathcal{H} = \sum_{\langle j,l \rangle}(-tc_j^\dagger c_l + \Delta e^{i\theta_{jl}}c_j c_l + h.c.) - \sum_j \mu c_j^\dagger c_j, \tag{A.1}$$

where t is the hopping amplitude, Δ is the amplitude of (2D) p-wave pairing, μ is the chemical potential, θ_{jl} is the polar angle of $\mathbf{r}_{jl} = \mathbf{r}_l - \mathbf{r}_j$, consistent with $\{c_l^\dagger, c_j^\dagger\} = 0$.

We will now include a gauge potential via a Peierls substitution as

$$c_j^\dagger \to c_j^\dagger \exp\left(-\frac{ie}{\hbar}\int_0^{\mathbf{r}_j} \mathbf{A} \cdot d\mathbf{l}\right),$$

$$c_j^\dagger c_l \to c_j^\dagger c_l \exp\left(\frac{ie}{\hbar}\int_{\mathbf{r}_j}^{\mathbf{r}_l} \mathbf{A} \cdot d\mathbf{l}\right)$$

$$\to c_l^\dagger c_j e^{i\phi_{j,l}}.$$

$$\phi_{jl} = \frac{e}{\hbar}\int_{\mathbf{r}_j}^{\mathbf{r}_l} \mathbf{A} \cdot d\mathbf{l} = -\phi_{lj} \tag{A.2}$$

The modified Hamiltonian is then

$$\mathcal{H} = \sum_{\langle j,l \rangle}(-te^{i\phi_{jl}}c_j^\dagger c_l + \Delta e^{i\theta_{jl}}c_j c_l + h.c.) - \sum_j \mu c_j^\dagger c_j, \tag{A.3}$$

The complex fermion operator can be written in the Majorana Fermion basis, a superposition of two Majorana fermions $c_j = \frac{1}{2}(a_j + ib_j)$. Due to the nature of Majorana fermions, $a_j^\dagger = a_j$, the creation operator is $c_j^\dagger = \frac{1}{2}(a_j - ib_j)$. It is quickly seen after substitution we arrive at

$$c_j^\dagger c_j = \frac{1}{2}(1 + ia_j b_j),$$ (A.4)

$$c_j^\dagger c_l = \frac{1}{4}(a_j a_l + b_j b_l + ia_j b_l - ib_j a_l),$$ (A.5)

$$c_j c_l = \frac{1}{4}(a_j a_l - b_j b_l + ia_j b_l + ib_j a_l).$$ (A.6)

The hopping term in MF basis are

$$-t(e^{i\phi_{jl}} c_j^\dagger c_l + e^{-i\phi_{jl}} c_l^\dagger c_j) = -\frac{it}{2}(\sin\phi_{jl}(a_j a_l + b_j b_l) + \cos\phi_{jl}(a_j b_l - b_j a_l)),$$ (A.7)

the order parameter terms are

$$\Delta(e^{i\theta_{jl}} c_j^\dagger c_l^\dagger + e^{-i\theta_{jl}} c_j c_l) = \frac{i\Delta}{2}(\sin\theta_{jl}(a_l a_j - b_l b_j) + \cos\theta_{jl}(a_l b_j + b_l a_j)).$$ (A.8)

Our Hamiltonian in MF basis is then

$$\mathcal{H} = -\frac{i}{2}\sum_{\langle j,l\rangle}[(t\sin\phi_{jl} - \Delta\sin\theta_{jl})a_j a_l + (t\sin\phi_{jl} + \Delta\sin\theta_{jl})b_j b_l$$

$$+(t\cos\phi_{jl} - \Delta\cos\theta_{jl})a_j b_l - (t\cos\phi_{jl} + \Delta\cos\theta_{jl})b_j a_l]$$

$$-\frac{i\mu}{2}\sum_j a_j b_j$$ (A.9)

For concreteness we consider a 1-D chain in the Kitaev limit $t = \Delta$, $\mu = 0$, and choose $phi_{jl} = 0$ (either zero or a perpendicular gauge potential). The Kitaev chain is resultant with $\mathcal{H} = -\sum_{j,j+1} it b_j a_{j+1}$ and hosting MZM a_1 and b_N.

A.2 Conditions for MZM on equilateral triangular islands

We want to now use a gauge potential to tune our system into having zero modes located at the base corners of a triangular lattice. Consider first forming a minimal Kitaev triangle in the positive y-axis, with only 3-sites such that its base, with sites 1 and 2, are along the x-axis. While still considering the Kitaev limit in this minimal model, as previously stated, sites 1 and 2 form a Kitaev chain. In order for the MZM to persist in the presence of site 3, one can choose ϕ_{23} and ϕ_{31} so that all terms involving these Majorana operators cancel out. For example, consider the 2–3 bond, for which $\theta_{23} = 2\pi/3$, we require

$$\sin \phi_{jl} + \sin \frac{2\pi}{3} = \cos \phi_{jl} + \cos \frac{2\pi}{3} = 0 \tag{A.10}$$

which means $\phi_{23} = -\pi/3$. Similarly one can find $\phi_{31} = -\phi_{13} = -\pi/3$. The three Peierls phases can be realized by the following staggered vector potential

$$\mathbf{A} = [1 - 2\Theta(x)] \frac{2\pi}{3\sqrt{3}} \hat{\mathbf{y}}. \tag{A.11}$$

Which is derived in the following subsection

A.2.1 Staggered vector potential

First, naively consider a constant vector potential field. For sites 1–2 we want the field to be perpendicular to their axis this tells us to start with $\mathbf{A} = A\hat{\mathbf{y}}$. From Eq. A.2, set $e = \hbar = 1$ and the

line integral for ϕ_{13} becomes

$$\phi_{13} = \int_{\mathbf{r_1}}^{\mathbf{r_3}} \mathbf{A} \cdot d\mathbf{l}$$

$$= A \int_{y_1}^{y_3} \hat{\mathbf{y}} \cdot d\mathbf{l}$$

$$= A \int_0^{\sqrt{3}a/2} dy$$

$$= \frac{\sqrt{3}Aa}{2}$$

$$= \pi/3.$$

We find that we need

$$A = \frac{2\pi}{3\sqrt{3}a}. \tag{A.12}$$

Now let us check if this allows for $\phi_{23} = -\pi/3$.

$$\phi_{23} = \int_{\mathbf{r_2}}^{\mathbf{r_3}} \mathbf{A} \cdot d\mathbf{l}$$

$$= A \int_{y_2}^{y_3} \hat{\mathbf{y}} \cdot d\mathbf{l}$$

$$= A \int_0^{\sqrt{3}a/2} dy$$

$$= \frac{\sqrt{3}Aa}{2}$$

$$= \frac{\sqrt{3}a}{2} \frac{2\pi}{3\sqrt{3}a}$$

$$= \pi/3 \neq -\pi/3.$$

Here we see that a constant vector potential does not meet the condition for MZM, it's off by a sign factor. This is remedied by using the Heaviside function instead from equation A.11

$$\mathbf{A} = [1 - 2\Theta(x)]\frac{2\pi}{3\sqrt{3}}\hat{\mathbf{y}}.$$

A.2.2 Linear vector potential

While the simplest vector potential one can use in the minimal Kitaev triangle is a staggered potential it remains to be seen if other odd functions also work. Again, we want the Peierls phase for sites 1–2 to have no contribution, let $\mathbf{A} = Ax\hat{\mathbf{y}}$. Simlarly, for sites 1–3 we have

$$
\begin{aligned}
\phi_{13} &= \int_{\mathbf{r_1}}^{\mathbf{r_3}} \mathbf{A} \cdot d\mathbf{l} \\
&= \int_{y_1}^{y_3} Ax \, dy \\
&= \int_{x_1}^{x_3} Ax \frac{dy}{dx} dx \\
&= \sqrt{3}A \int_{-a/2}^{0} x \, dx \\
&= -\frac{\sqrt{3}Aa^2}{8} \\
&= \pi/3.
\end{aligned}
$$

The magnitude is then

$$A = -\frac{8\pi}{3\sqrt{3}a^2}. \tag{A.13}$$

Check if $\phi_{23} = -\pi/3$:

$$\phi_{23} = \int_{x_2}^{x_3} Ax \frac{dy}{dx} dx$$

$$= -\sqrt{3}A \int_{a/2}^{0} x dx$$

$$= A \left(\frac{\sqrt{3}a^2}{8} \right)$$

$$= -\frac{8\pi}{3\sqrt{3}a^2} \left(\frac{\sqrt{3}a^2}{8} \right)$$

$$= -\pi/3.$$

We have shown a linear vector potential (symmetric/centered about the y-axis) can host MZM on a minimal Kitaev triangle's base corners. In general, this should be true for any odd function used

Triangle Length and Vector Potential Strength

For a staggered vector potential such as a Heaviside or Tanh function we do not need to adjust the vector potential strength relative to its size. When considering larger Kitaev triangles we need to adjust the vector potential strength for linear and higher order vector potentials. Start with the botton left corner point, x_j, and look at its nearest neighbor along $\theta = \pi/3$, we denote this point with position x_l. If we look back at the line integral of a linear function we have the general form of

$$\phi_{jl} = A \int_{x_j}^{x_l} \frac{dy}{dx} x dx$$

$$= \frac{\sqrt{3}A}{2}(x_l^2 - x_j^2) = \pi/3.$$

We can rearrange to get

$$A = \frac{2\pi}{3\sqrt{3}} \frac{1}{x_l^2 - x_j^2}. \tag{A.14}$$

A more simplified solution follows. For the outer length of a triangle we use `nr` to denote the number of rows the triangle has, it is one of the first few defined variables in a given script. The positions x_j and x_l have simple linear relations in regards to `nr`. Due to the equilateral nature of our triangle and centering about the y-axis

$$x_l = \frac{-a}{2}(\text{nr} - 1). \tag{A.15}$$

It's easy to see that $x_l = x_j + a/2$ which gives

$$x_l = \frac{-a}{2}(\text{nr} - 2). \tag{A.16}$$

Now, the difference of the squares is

$$x_l^2 - x_j^2 = \frac{-a^2}{4}(2\text{nr} - 3). \tag{A.17}$$

Plugging back into our expression we find

$$-\frac{8\pi}{3\sqrt{3}a^2(2\text{nr} - 3)}. \tag{A.18}$$

This is expression is easy to implement in code.

Bibliography

Bibliography